OPTOELECTRONICS AND ADVANCED MATERIALS – RAPID COMMUNICATIONS Vol. 19, Iss. 7-8, July-August 2025, p. 318 - 327

Simulation and modeling of supercontinuum generation in GAST chalcogenide PCF

T. MESBAHI[1,2], A. MEDJOURI[1,*]
[1]*LEVRES Laboratory, Faculty of Exact Sciences, University of El Oued, 39000 El Oued, Algeria*
[2]*LABTHOP Laboratory, Faculty of Exact Sciences, University of El Oued, 39000 El Oued, Algeria*

The supercontinuum (SC) generation in chalcogenide Photonic crystal fiber (PCF) offers unique opportunities for mid-infrared light sources due to the broad transparency window of chalcogenide materials and the high nonlinearity. In this work, we analyze and design a $Ge_{20}As_{20}Se_{17}Te_{43}$ chalcogenide PCFs for broadband SC generation in the all-normal dispersion regime. The SC generation was carried out using numerical modelling by solving the generalized nonlinear Schrödinger equation (GNLSE). Our results show that the SC spans 2.9–13.95 μm at -5 dB with stable and highly coherent spectra. These results provide guidelines for future experimental efforts and the design of chalcogenide fibers tailored for specific SC applications in spectroscopy and frequency metrology.

(Received November 24, 2024; accepted August 4, 2025)

Keywords: Photonic crystal fibers, Supercontinuum generation, Nonlinear optics, Chalcogenides, Spectroscopy

---

1. Introduction

The significant spectrum broadening produced by ultrafast laser pulses propagating in nonlinear media is known as supercontinuum (SC) production, through linear and nonlinear processes in the medium [1]. In 1970, Alfano and Shapiro made the first discovery of SC generation was in glass with non-linear properties. As a result of this pioneering experience, the SC has been widely employed in numerous applications of several fields [2], such as the differential optical absorption spectroscopy (DOAS) system [3], optical coherence tomography (OCT) [4], industrial applications [5], biomedical imaging, material processing and optical sensing [6], frequency metrology [7].

SC has been generated in various types of nonlinear media, including, gases, inorganic and organic liquids, solids, and numerous waveguide kinds [1,2]. In optical waveguides, the production of spectrally continuous radiation by femtosecond pumping is influenced by many nonlinear and linear processes, and it is closely tied to the dispersion profile shown by the optical waveguide [8]. Generally speaking, when pumping optical pulses with the anomalous dispersion regime, the SC process is caused by soliton dynamics, Raman self-frequency shifting and dispersive wave generation. Due to the effect of sensitivity to noise amplification and resulting shot-to-shot variations, the spectra of SC are not completely coherent [9,10]. On the other hand, when pumping occurs in the normal dispersion regime, self-phase modulation (SPM) and optical wave breaking (OWB) dominate the spectrum broadening dynamics. Here, the resulting spectrum of SC exhibits high coherence, flattop wideband spectral profiles and stability. However, it is narrower compared to the output obtained in the anomalous dispersion regime [11,12].

At the end of the 1990s, a new class of optical waveguides appeared, called photonic crystal fibers (PCF) or microstructured optical fibers [13]. They have garnered significant attention because of their potential to enable novel pathways for optical devices and related technologies, such as SC [14,15]. When compared to traditional optical fibers, PCFs have a large contrast in the refractive index and endlessly single-mode operation [16]. Moreover, PCFs provides a very suitable medium for SC generation due to ease of engineering dispersion in the mid-infrared and good nonlinear characteristics [17,18]. Accordingly, many studies have been done for soft glass PCFs fluoride, chalcogenide and tellurite due to strong nonlinear Kerr effect and their extensive transparency in the mid-infrared region [19]. Systems of chalcogenide glasses are non-oxide, mainly consists of one or more elements for example Sulfur (S), Tellurium (Te), and Selenium (Se) (chalcogen elements), in combination with other metalloid components for example antimony (Sb), germanium (Ge), arsenic (As), etc. They have a transparency window exceeding over 20 μm for some compositions with minimal two-photon absorption in this region. Furthermore, the optical nonlinearity of chalcogenide glasses systems is up to a hundred times greater than that of tellurite glasses [20] and a thousand times greater than silica glasses [21] by employing chalcogen elements, lanthanum, sulphide and gallium was used to create the first chalcogenide glass PCF [22]. Owing to its outstanding optical properties, Glasses based on chalcogenides are found suitable for applications in the mid-infrared range such as SC [20].

The SC produced in chalcogenide waveguides has been expanded quickly [23], especially in PCF based on chalcogenide and many designs with different chalcogenide glass compositions have been thoroughly investigated [24]. Furthermore, PCF based on chalcogenide glass can be easily obtained all-normal dispersion regime (ANDi) in the mid-infrared. In fact, the SC spectrum achieved in the ANDi regime exhibits high coherence, flat-top wideband spectral profile and excellent stability. Interestingly, the generation of new spectral components is obtained in a deterministic fashion due the absence of modulation instability effect. In this regard, the experimental and theoretical study of SC generation has received much attention in recent years, especially in the PCF with ANDi [25]. For example, Yan et al. reported SC perfect coherent properties in mid-infrared spanning from 2 μm to 5 μm with 50 fs duration of pulse and 1000 W peak power by pumping at wavelength 3 μm in As_2S_3 chalcogenide glass PCF [26]. Seyed et al. demonstrated, via numerical simulations, SC generation spanning a range of 4.97 μm with perfect coherence at 20 dB and 4.14 μm at 8 dB in $AsSe_2$ PCF. The SC generation is realized by pumping 50 fs duration of pulses and low peak power of 1000 W at wavelength 6.9 μm [27]. Diouf et al., numerically demonstrated SC with highly coherent mid-infrared extending in the range 2.9 - 4.575 μm at 3 dB in $As_{38.8}Se_{61.2}$ glass PCF with pump wavelength 3.7 μm, 50 fs pulses with and 0.88 KW peak power in a 5 cm PCF length [28]. Moreover, SC in mid-infrared spanning from 1.5 to 12.2 μm has been demonstrated in 1 mm of $AsSe_2$ PCF with 100 fs duration and 1.3 nJ energy laser pulses pumped at 3.5 μm [29]. Karim et al. achieved coherent SC generation expanding from 2 - 5.5 μm by pumping at wavelength 3100 nm into a 0.1 cm length PCF made of $Ge_{11.5}As_{24}Se_{64.5}$ glass with a peak power 5 KW [30]. Medjouri et al. reported SC highly coherent in mid-infrared covering 1.45 - 5.95 μm by using a 15 mm-long GeS_2-Ga_2S_3-CsI glass PCF with 50 fs duration and 3 nJ energy optical pulses pumped at the wavelength 3 μm [31].

Over the past few years, different materials, Glasses based on chalcogenide for example Ge-Sb-Se or Ge-As-Se have been utilized in SC generation, where SC spectra spanning the range of 1.8 to 14 μm have been demonstrated [32]. While SC generation is based on high optical nonlinearity, practically, the optical materials' nonlinear properties can be enhanced and the transparency extended to far longer wavelengths by substituting a lighter chalcogen element with a heavier one [33]. In comparison to chalcogenide glasses based on sulfur (S) or selenium (Se), chalcogenide glasses based on tellurium (Te) are of highly interest for mid-infrared SC generation as they exhibit larger optical nonlinearities and the much wide transmission windows because of the heaviness of the Te atom [34,35]. But, to avoid the tendency to crystallization due to the properties of Te, the small quantity of Te in chalcogenide glasses can be replaced by Se to increase the resistance to crystallization while keeping a broad window of optical transmission [36]. The first experimental investigation of SC generation in chalcogenide glasses based on tellurium (Te) has been reported by Zhao et al. [37]. The authors demonstrated mid-infrared SC generation extending from 1.5 - 14 μm in chalcogenide glasses based on tellurium (Te) step-index conventional fiber with pump wavelength 4.5 μm, 0.88 kw peak power and 150 fs pulse duration, achieved within a fiber length of 23 centimeters [37]. Recently, Jing Xiao et al., employed Ge-As-Se-Te chalcogenide glasses (GAST) to achieve SC generation [38]. The authors reported SC spectra spanning from 3.5 to 10.5 μm at 5 μm wavelength in 19 cm-long double-clad fiber by pumping 150 fs duration optical pulses.

In this work, we provide a rigorous modeling of the SC generation process in single-mode PCFs. We choose the $Ge_{20}As_{20}Se_{17}Te_{43}$ as a solid background glass, and this owing to its excellent properties such as long-wave IR transparency and easiness to obtain an ANDi regime due to larger material zero-dispersion-wavelength (ZDW) [37,38]. Besides, we propose a PCF design of with a Circular Lattice (CL-PCF). This CL-PCF is described by six rings to ensure well light confinement within the core of the fiber. The numerous linear and nonlinear properties are accurately computed for various wavelengths through the application of the finite difference frequency domain (FDFD) method in combination with the perfectly matched layers (PML) boundary condition. Besides, optical pulses propagation and SC generation process are both modeled by numerically solving the generalized nonlinear Schrödinger equation (GNLSE).

2. Theoretical background

2.1. Structure of GAST based CL-PCF

Here, we propose a design of a CL-PCF structure with six rings of air holes. Fig. 1 illustrates the transverse cross-sectional structure of the design. In this structure, we select the $Ge_{20}As_{20}Se_{17}Te_{43}$ Chalcogenide glass as a solid background material. The distance between two neighboring holes of air, commonly known as the pitch, is 3 μm, the first two rings have diameters of air holes d_1 equal to 1.4 μm and from the third ring to the sixth ring, the air hole diameters d_2 vary between 1 μm and 1.5 μm, increasing in steps of 0.1 μm. The diameters of air hole and the number of rings is carefully selected to achieve well waveguiding within the core with a slight confinement loss and changing d_2 to engineer the dispersion in regime ANDi. Moreover, The PCF used in this study is designed with a small air hole diameter-to-pitch ratio, satisfying the condition for endlessly single-mode operation. Furthermore, and based on the numerical mode analysis, only the fundamental mode is supported across the operational wavelength range. This justifies the single-modenness of the fiber. Besides, the proposed GAST based CL-PCF can be fabricated by a conventional method and drawing at 310 °C [38, 39].

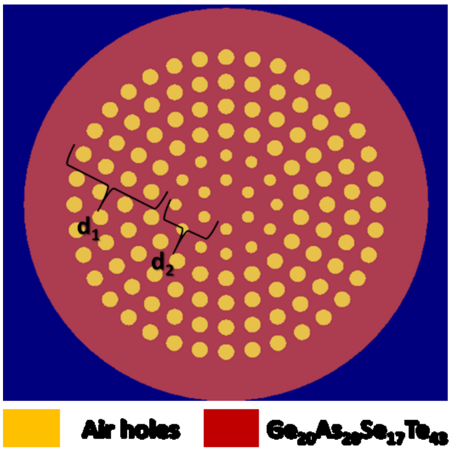

Fig. 1. Transverse cross section of $Ge_{20}As_{20}Se_{17}Te_{43}$ glass CL-PCF (colour online)

2.2. Linear and nonlinear parameters computation

We use a complete vector finite-difference frequency-domain method (FV-FDFD) combined by perfectly matched layers (PML) as a boundary condition to simulate CL-PCF properties. In this case, the Maxwell's equations can be expressed as [40, 41]:

$$\begin{aligned} ik_0 s\varepsilon_r E &= \nabla \times H \\ -ik_0 s\varepsilon_r H &= \nabla \times E \end{aligned} \tag{1}$$

$$s = \begin{pmatrix} \frac{S_x}{S_y} & & \\ & \frac{S_x}{S_y} & \\ & & S_x S_y \end{pmatrix} \tag{2}$$

where: $S_x = 1 - (\sigma_x / i\omega\varepsilon_0)$ and $S_y = 1 - (\sigma_y / i\omega\varepsilon_0)$

E is the electric field, H is magnetic field, k_0 is the wavenumber in the vacuum, ε_0 is the vacuum permittivity, ω is the angular frequency and σ is the conductivity [42]. An appropriate meshing system for the structure of PCF converts the equation system presented in (1) into a matrix eigenvalue problem. The numerical solution is achieved using the sparse matrix method to determine the optical field distribution and the effective refractive index n_{eff} [40]. We can calculate the refractive index values using the Sellmeier equation, which represents the relationship between the wavelength and the material's optical properties [38]:

$$n = 1 + \sum_j \frac{A_j \lambda^2}{\lambda^2 - \lambda_j^2} \tag{3}$$

where λ represents the wavelength. A_j and λ_j are the Sellmeier coefficient. Table 1 shows the values A_j and λ_j of (GAST) glasses.

Table 1. Sellmeier coefficients of GAST glass

A_j $(j = 1, 2, 3)$	λ_j^2 (j=1, 2, 3)
8.7503	0.39859
$3.425.10^{-4}$	191.88
-25.56	−17840

The chromatic dispersion is essential in determining the SC spectrum [43]. It results from the contribution of two sources: the dispersion of the material and the waveguide, denoted by D and given by [44]:

$$D(\lambda) = -\frac{\lambda}{c}\frac{d^2 n_{eff}}{d\lambda^2} \tag{4}$$

where n_{eff} is the effective refractive index, λ is the wavelength, c is the speed of light in a vacuum, and c is the velocity of light in a vacuum.

The confinement loss (L_c) for the fundamental mode in the fiber can be expressed as [45]:

$$L_c = \frac{20}{\ln(10)} \frac{2\pi}{\lambda} Im(n_{eff}) \tag{5}$$

where the variable $Im(n_{eff})$ represents the imaginary part of the effective index.

A significant factor in the generation of SC is the nonlinear coefficient (γ). It can be calculated with the formula below [46]:

$$\gamma = \frac{n_2 \omega_0}{c A_{eff}} \tag{6}$$

where the nonlinear refractive index is represented by n_2 of $Ge_{20}As_{20}Se_{17}Te_{43}$ glass is calculated as [38]:

$$n_2 = 4.27 \times 10^{-16} \frac{(n_0^2 - 1)^4}{n_0^2} [cm^2.w^{-1}] \tag{7}$$

where n_0 is the linear refractive. Moreover, A_{eff} represents the effective area of the fundamental mode, defined as [47].

$$A_{eff} = \frac{(\iint |F(x,y) dxdy|)^2}{\iint |F(x,y)|^4 dxdy} [\mu.m^2] \tag{8}$$

with $F(x, y)$ is the distribution of fundamental mode in fiber.

2.3. Modelling of pulses propagation and SC generation

This work aims to generate a supercontinuum (SC) in the mid-infrared range. We employ the generalized nonlinear Schrödinger equation (GNLSE). This equation illustrates the contributions of both linear and nonlinear processes [48, 49]:

$$\frac{\partial A}{\partial Z} + \frac{\alpha}{2} A - \sum_{n \geq 2} \frac{i^{n+1}}{n!} \beta_n \frac{\partial^n A}{\partial T^n} = i\gamma(1 - f_R)$$
$$\left([A]^2 A - \frac{i}{\omega_0} \frac{\partial}{\partial T} [A]^2\right) + i\gamma f_R \left(1 + \frac{i}{\omega_0}\right)$$
$$\left(A \int_0^\infty h_R(\tau) |A(z, T - \tau)|^2 \partial\tau\right) \tag{9}$$

The first side represents the linear propagation effects, where A is the pulse envelope function, α is the coefficient of attenuation, β_n represents the dispersion of the nth order, and ω_0 is the input pulse frequency. The second side represents the nonlinear effects, γ is the nonlinear coefficient. Finaly, $h_R(t)$ is the delayed Raman contribution shown as [50]:

$$h_R(t) = \frac{\tau_1^2+\tau_2^2}{\tau_1\tau_2}\exp(-\frac{t}{\tau_2})\sin(\frac{t}{\tau_1}) \qquad (10)$$

where τ_1 = 15.2 fs and τ_2 = 230.5 fs, and $f_R = 0.031$ is the fractional Raman response contribution [38], resulting from the normalization of $\int_0^\infty h_R(t)dt = 1$ [51] .

Many methods have been reported to solve the GNLSE. The technique used in our simulations is called the Runge-Kutta in the interaction picture (RK4IP) method. This method is chosen for its high numerical accuracy and local error of fifth-order O (h5) with a global error of only O(h4). The RK4IP and Split Step Fourier Method (SSFM) are closely linked [48]. In the RK4IP method, the dispersion and nonlinear operators are defined as follows:

$$\widehat{D} = \frac{\alpha}{2}A - (\sum_{n\geq 2}\beta_n \frac{i^{n+1}}{n!}\frac{\partial^n A}{\partial T^n})A \qquad (11)$$

$$\widehat{N} = i\gamma\left(1+\frac{i}{\omega_0}\frac{\partial}{\partial T}\right)\times$$
$$\times\left((1-f_R)A|A|^2 + f_R A\int_0^\infty h_R(\tau)|A(z,t-\tau)|^2\partial\tau\right) \qquad (12)$$

by transforming the pulse envelope A into the interaction picture A_I, we can write:

$$A_I = \exp\left(-(z-\grave{z})\widehat{D}\right)A \qquad (13)$$

$\grave{z}$ denotes the separation distance between the interaction and normal pictures of the pulse envelope A . Differentiating (13) gives the evolution of A_I:

$$\frac{\partial A_I}{\partial z} = \widehat{N}_I A_I \qquad (14)$$

where $\widehat{N}_I$ is the nonlinear operator in the interaction picture given by:

$$\widehat{N}_I = \exp\left(-(z-\grave{z})\widehat{D}\right)\widehat{N}\exp\left(-(z-\grave{z})\widehat{D}\right) \qquad (15)$$

with a spatial step h, the RK4IP algorithm advances $A(z,t)$ to $A(z+h,t)$ which is expressed as follows [52]:

$$A_I = \exp(\frac{h}{2}\widehat{D})A(z+h,t) \qquad (16)$$

$$K_1 = \exp(\frac{h}{2}\widehat{D})\left[h\widehat{N}A(z+h,t)\right]A(z+h,t) \qquad (17)$$

$$K_2 = \mathrm{h}\widehat{N}(A_I+\frac{K_1}{2})\left[A_I+\frac{K_1}{2}\right] \qquad (18)$$
$$K_3 = \mathrm{h}\,\widehat{N}\left(A_I+\frac{K_2}{2}\right)\left[A_I+\frac{K_2}{2}\right] \qquad (19)$$

$$K_4 = \mathrm{h}\,\widehat{N}\left[\left(\frac{h}{2}\widehat{D}\right)(A_I+K_3)\right]\times\exp\left(\frac{h}{2}\widehat{D}\right)[(A_I+K_3)] \qquad (20)$$

$$A(z+h,t) = \exp\left(\frac{h}{2}\widehat{D}\right)\left[A_I+\frac{K_1}{6}+\frac{K_2}{3}+\frac{K_3}{3}\right]+\frac{K_4}{6} \qquad (21)$$

In general, the computational algorithm of the RK4IP method is considered the most efficient and accurate for modeling pulse propagation into optical fibers [53, 54]. Coherence is an essential parameter for determining the quality of the SC, the first-order degree of coherence given by [55]:

$$|g_{12}^1(\lambda, t_1-t_2)| = \left|\frac{\langle E_1^*(\lambda,t_1)E_2(\lambda,t_2)\rangle}{\langle|E_1(\lambda,t_1)|^2\rangle\langle|E_2(\lambda,t_2)|^2\rangle}\right| \qquad (22)$$

where E_1, E_2 are the electric fields, and the variable t represents the time measured according to the temporal resolution of the spectrometer used to resolve the spectra. We use $t_1 - t_2 = 0$ to obtain the coherence $|g_{12}^1(\lambda)|$ depending on the wavelength. When $|g_{12}^1(\lambda)| = 1$, the coherence of SC is perfect [56].

3. Simulation results and discussion

3.1. Dispersion engineering of GAST PCF

Fig. 2 depicts the refractive index variation of GAST versus wavelength in the range of 2 µm to 12 µm, using the Sellmeier model. The refractive index curve of GAST shows a decreasing pattern as the wavelength increases from 2 µm to 12 µm, with values ranging from 3.23 to 2.9. This corresponds with measurements taken by an IR ellipsometer (IR-VASE MARK II, J. A. Woollam Co.) [38].

To achieve the ANDi property of the suggested CL-PCF, we adjusted the dispersion by changing the diameter of the first two rings of air holes d_2 while keeping Λ=3 µm and d_1=1.4 µm. Fig. 3 illustrates the variation of dispersion as a function of wavelength between 2 µm and 12.5 µm, with d_2 varying from 1 µm to 1.5 µm in increments of 0.1 µm, demonstrating the effect of changing d_2 on the dispersion of the suggested PCF. As can be observed, when d_2 increases, the dispersion curve shifts upward, and the ANDi regime is readily achieved at d = 1.3 µm with a peak close to zero obtained around the wavelength 5.8 µm.

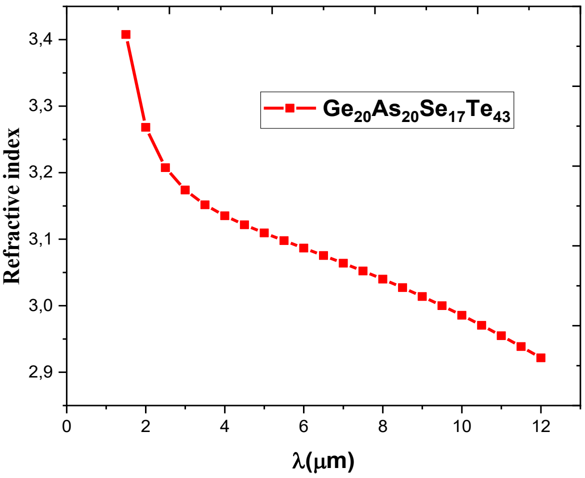

Fig. 2. Refractive index of the $Ge_{20}As_{20}Se_{17}Te_{43}$ (GAST) versus wavelength

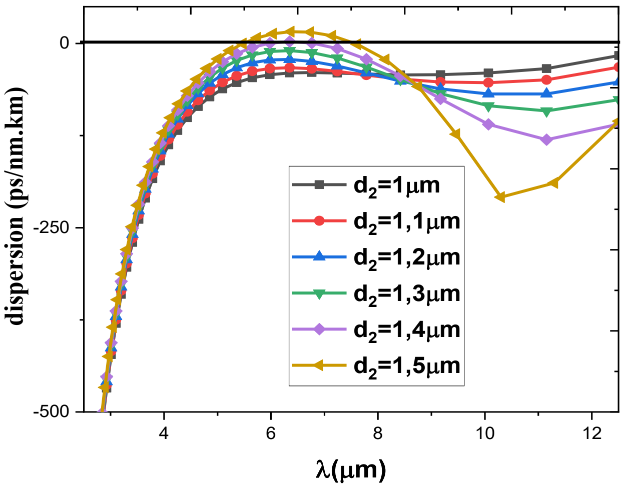

Fig. 3. Dispersion dependent wavelength with Λ = 3 μm, d_1=1.4 μm and d2 varies (colour online)

Furthermore, Fig. 4 depicts the confinement loss (L_C) dependent wavelength. As shown in this figure, the confinement loss curve shows that the optical (GAST) PCF material is suitable for pumping at a wavelength of 5.8 μm. The curve demonstrates that the loss remains very low from 2 to 9 μm, indicating strong energy confinement within this wavelength range and making the material effective for energy transmission, especially at 5.8 μm. Beyond 9 μm, optical losses begin to increase, indicating a decrease in efficiency outside this range.

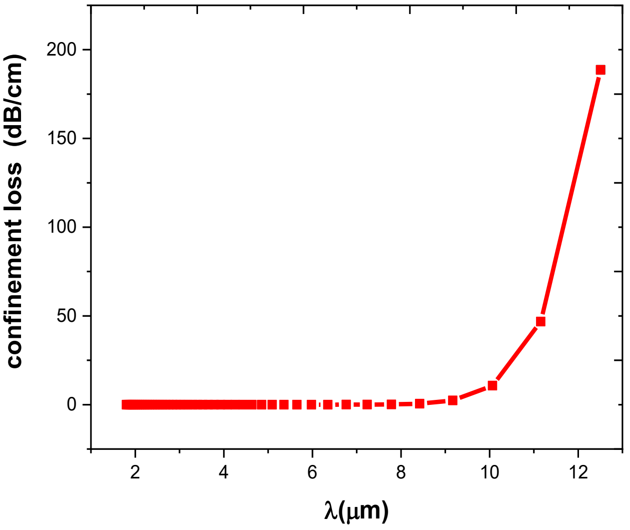

Fig. 4. The confinement loss dependent wavelength with Λ = 3 μm, d_1=1.4 μm and d_2=1.3 μm

Finally, both the effective area of the fundamental mode, A_{eff}, and the nonlinear coefficient, γ, are calculated and shown in Fig. 5. The GAST PCF shows a decrease in the Kerr coefficient with increasing wavelength, while the effective area increases, indicating wider field spread. The Kerr coefficient is about 1,495 $m^{-1}.W^{-1}$ at the chosen pump wavelength of 5.8 μm, demonstrating high nonlinearity at this wavelength.

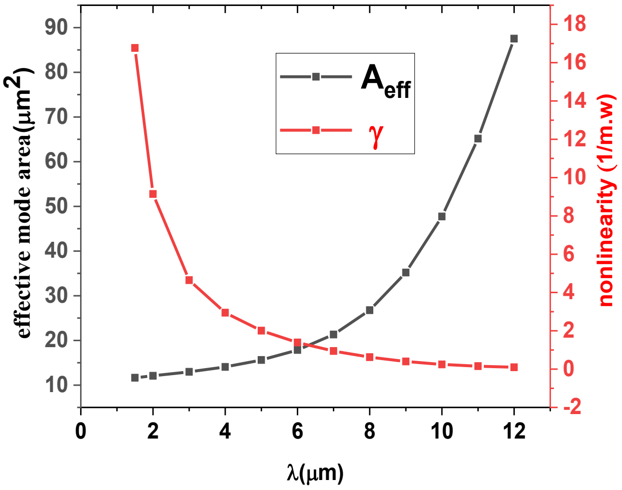

Fig. 5. The nonlinear coefficient and effective area vary with wavelength (colour online)

3.2. The SC generation in a GAST PCF design

To investigate SC generation in our optimized PCF design, we numerically solve the Generalized Nonlinear Schrödinger Equation (GNLSE) as described by Eq. (7). Optical pulses within the core of the GAST PCF are modeled with a hyperbolic secant envelope $A(z,t) = \sqrt{P_0}\mathrm{sech}(t/T_0)$, Here, P_0 represents the peak power and T_{FWHM} = 1.763 T_0 denotes the pulse duration. The wavelength of the laser pulses is 5.8 μm, close to the wavelength of zero dispersion. Such optical pulses can be generated from sources realized through nonlinear frequency conversion techniques, particularly using Optical Parametric Oscillators (OPOs). For example, Zhang et al. (2013) demonstrated a femtosecond-laser-pumped $CdSiP_2$-based OPO that generated broadband mid-infrared idler pulses centered around 6.2 μm, with spectral coverage from 5.8 to 6.6 μm [57]. This work clearly shows the feasibility of generating femtosecond pulses in the 5.8 μm region using established nonlinear optical methods. Thus, the chosen pump wavelength in our simulation is both practically motivated and technically attainable with currently available laser and nonlinear materials.

The coefficients of the Taylor series expansion for the propagation constant have been calculated up to the ninth order at a wavelength of 5.8 μm for two dispersion regimes: the ANDi regime with d_2=1.3 μm in Table 2, and anomalous dispersion with d_2=1.5 μm in Table 3. Furthermore, the propagation loss is neglected in the GNLSE because the pulse propagates over only a short length of the PCF. Firstly, our objective is to compare SC outputs in two dispersion regimes. Fig. 6 presents a comparison of SC outputs in two dispersion regimes: the anomalous dispersion regime with d_2=1.5 μm (a) and the ANDi regime with d_2=1.3 μm (b). The SC output the anomalous dispersion regime is wide and has more spectral instabilities. On the other hand, the ANDi regime produces a smoother spectral output with fewer instabilities, even though its spectral width is narrower than that of the anomalous regime. This proves that the ANDi regime is crucial for achieving optimal SC production. The values of the parameters used in this simulation are P_0=1Kw, T_{FWHM}=150 fs and the GAST PCF has a length of 15 mm.

Table 2. The propagation constant for d2=1.3 μm

Coefficient	Value
β_2	253.841 ps^2/km
β_3	3.78122 ps^3/km
β_4	6.10128 $\times 10^{-02}$ ps^4/km
β_5	-1.0278 $\times 10^{-03}$ ps^5/km
β_6	1.10671 $\times 10^{-05}$ ps^6/km
β_7	-7.85847 $\times 10^{-8}$ ps^7/km
ß$_8$	3.44315 $\times 10^{-10}$ ps^8/km
ß$_9$	-7.08451 $\times 10^{-13}$ ps^9/km

Table 3. The propagation constant for d2=1.5 μm

Coefficient	Value
β_2	-187.085 ps^2/km
β_3	12.0773 ps^3/km
β_4	0.133769 ps^4/km
β_5	-8.62397 $\times 10^{-03}$ ps^5/km
β_6	2.21362 $\times 10^{-04}$ ps^6/km
β_7	-3.2625 $\times 10^{-6}$ ps^7/km
ß$_8$	2.73342 $\times 10^{-8}$ ps^8/km
ß$_9$	-1.02401 $\times 10^{-10}$ ps^9/km

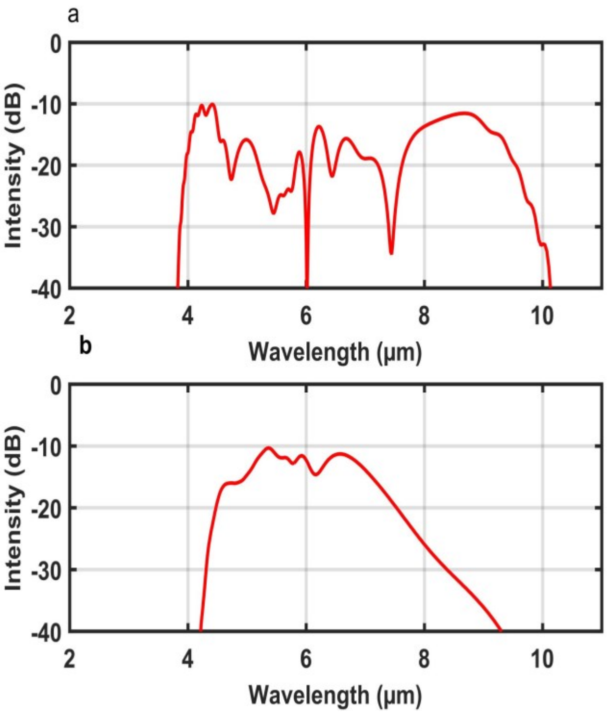

Fig. 6. SC generation in anomalous dispersion regime with d2=1.5 μm (a) and ANDi regime with d2=1.3 μm (b)

In order to explain the dynamics of SC broadening in the ANDi regime, the characteristic dispersive and nonlinear length scales are calculated by [2]: $L_D = T_0^2|\beta_2|^{-1} = 28.6\,mm$, $L_{NL} = (\gamma P_0)^{-1} = 0.67\,mm$, respectively. It can be observed that the dispersive length is longer than the nonlinear length, which makes the nonlinear dynamics responsible for spectral widening over the first few millimeters of the PCF. Fig. 7 shows the pulse evolution in both spectral and temporal domains with P_0 = 1 Kw and T_{FWHM} = 150 fs over the 15 mm length of the GAST PCF, as can be noted. Initially, the primary mechanism responsible for the symmetric spectral broadening of the pulse is self-phase modulation (SPM). Accordingly, the wave-breaking (OWB) distance is calculated as 5.3 mm using the formula [2]:

$$L_{OWB} = \sqrt{\frac{3\beta_2}{2\beta_2+2\gamma P_0 T_0^2}\frac{T_0^2}{\beta_2}} \tag{23}$$

The OWB effects become noticeable after 5.3 mm, where side lobes appear on both extremes of the spectrum, marking the onset of the OWB process. This analysis emphasizes the initial impact of SPM on spectral broadening, followed by wave-breaking effects as propagation distance increases.

3.2.1. Effect of the pump pulse initial conditions on the SC spectrum

In this section, we investigate the impact of the initial conditions of the pulses of the pump on the SC spectrum. Firstly, to show how the pulse duration affects the characteristics of the SC spectrum, particularly its bandwidth and flatness, we vary the pulse duration values to 200 fs (a), 150 fs (b), 100 fs (c), and 50 fs (d) with a peak power of 2 kW and pump wavelength 5.8 μm. As shown in Fig. 8, it is clear that for input pulse durations of 100 fs, 150 fs, and 200 fs, the width of the SC generation decreases. But a broadband and flat SC spectrum is observed with a 50 fs pulse duration, which extends from 4.18 to 9.2 μm at -10 dB in a 15 mm length of the PCF. Consequently, this short pulse duration is adopted for the remainder of the study to achieve broader and flatter spectra.

Secondly, Fig. 9 illustrates the effect of increasing pulse power on the generated SC bandwidth, with the pulse duration held constant at 50 fs and a pump wavelength of 5.8 μm. The peak power is varied at 1 kW, 5 kW, 10 kW, and 15 kW, respectively. It can be observed that the SC spectrum achieves maximum bandwidth and high flatness at a peak power of 15 kW, spanning the range from 2.9 to 13.95 μm at -5 dB in a 15 mm length of the PCF, as shown in Fig. 9(d).

3.2.2. Coherence of the generated SC

Fig. 10 illustrates the SC spectral coherence in a 15 mm PCF, achieved using a 5.8 μm pump, 50 fs pulse duration (T_{FWHM}), and 15 kW peak power. The SC spectrum exhibits perfect coherence in this range of wavelengths. This high spectral coherence is achieved by eliminating soliton effects through pumping in the normal regime of dispersion. Consequently, spectral broadening occurs primarily due to self-phase modulation (SPM), a deterministic process that maintains the coherence of the input pulses [7]. Table 4 depicts a summary of the simulation parameters used to generate the SC shown in Fig. 9(d). The proposed SC based on GAST PCF offers several advantages over previous works. The SC spans 2.9–13.95 µm at a -5 dB level with high stability and demonstrates high coherence, surpassing many earlier works in terms of spectral coverage [26-31, 52]. These excellent optical properties make the proposed SC spectrum highly suitable for several industrial and scientific applications.

Table 4. Optical parameters of the proposed SC source based on GAST PCF

Fiber length	15mm
Pump wavelength	5.8 µm
Peak power	15 kW
T_{FWHM}	50 fs
The bandwidth of SC	2.9-13.95
Flatness	-5 dB

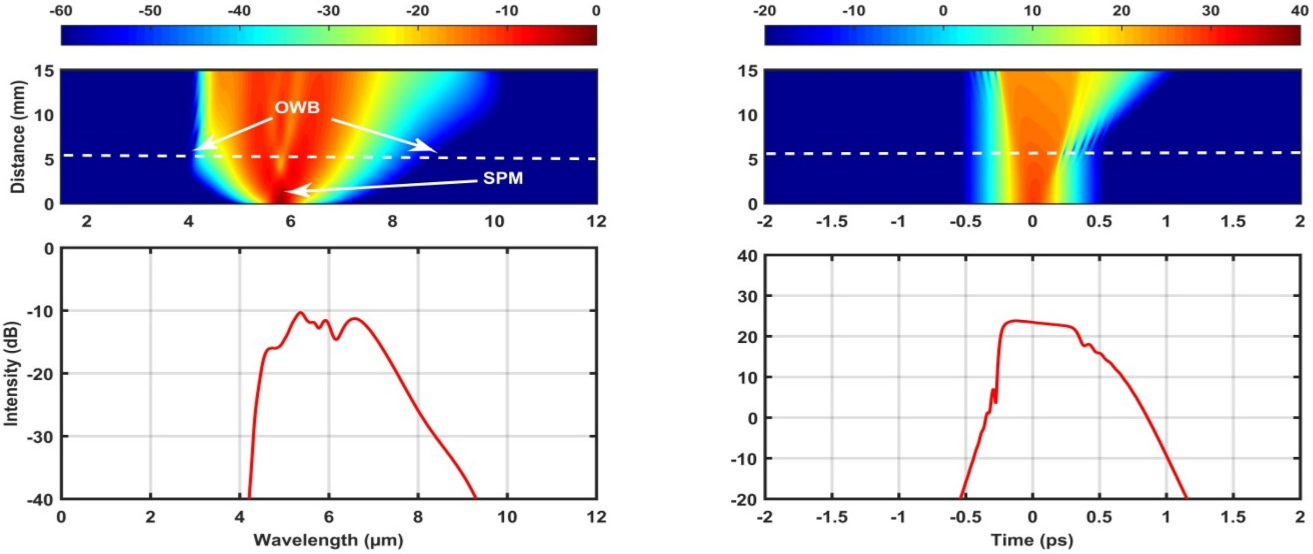

Fig. 7. Temporal and spectral evolution over a 15 mm length of PCF with pump wavelength 5.8 µm. P0=1 Kw, T_{FWHM}=150 fs. The beginning of the OWB process is at the dashed line (colour online)

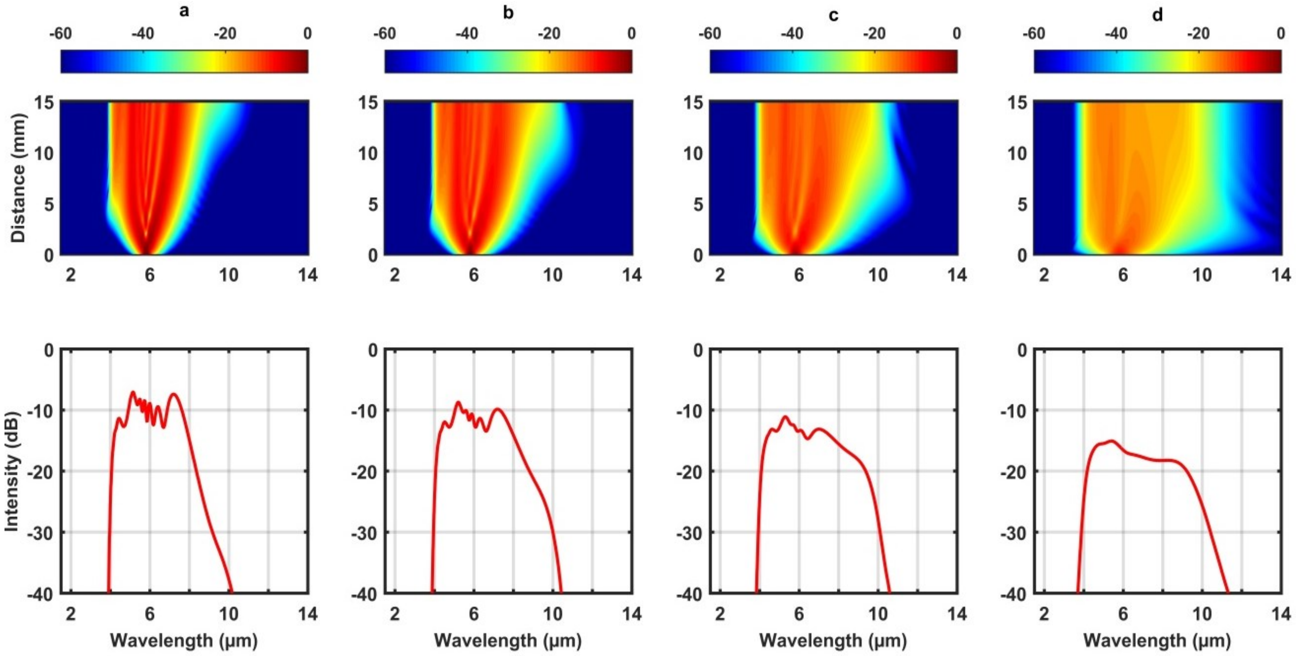

Fig. 8. SC spectrum generated in a 15 mm PCF with an input pulse peak power of 2 kW and varying pulse duration T_{FWHM} values of 200 fs (a), 150 fs (b), 100 fs (c), and 50 fs (d) (colour online)

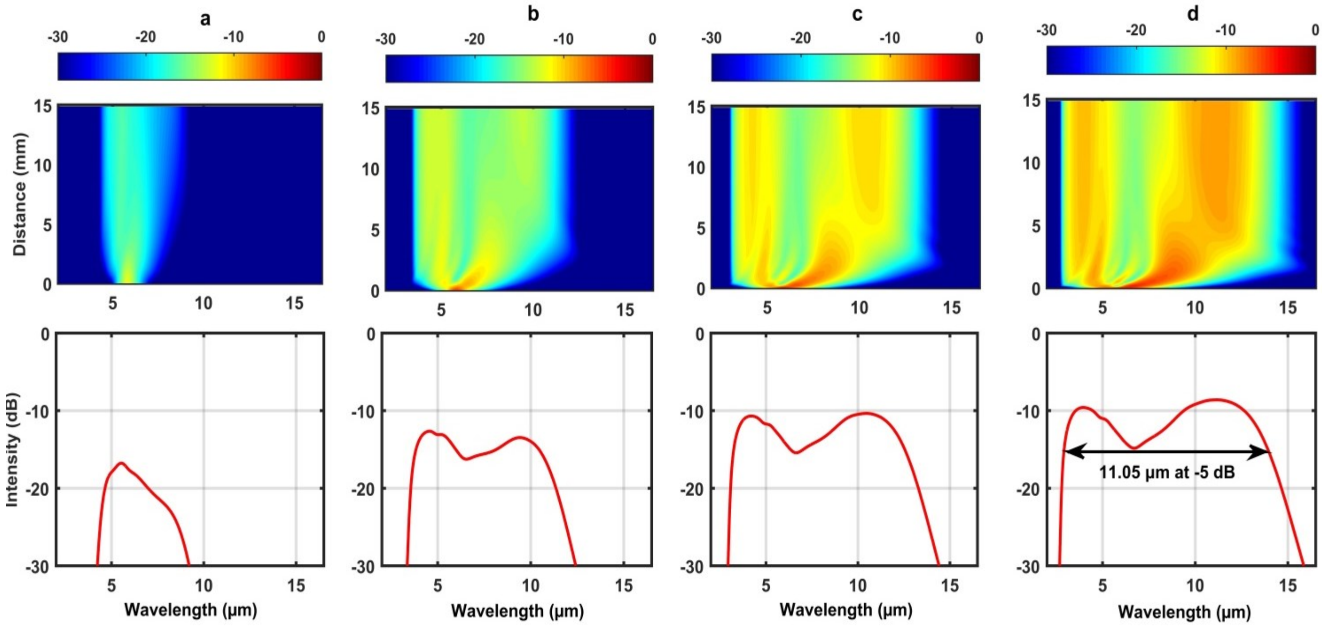

Fig. 9. Shows the SC spectrum generated in a 15 mm PCF with a 50 fs pulse duration (T_{FWHM}) and varying peak power values: 1 kW (a), 5 kW (b), 10 kW (c), and 15 kW (d) (colour online)

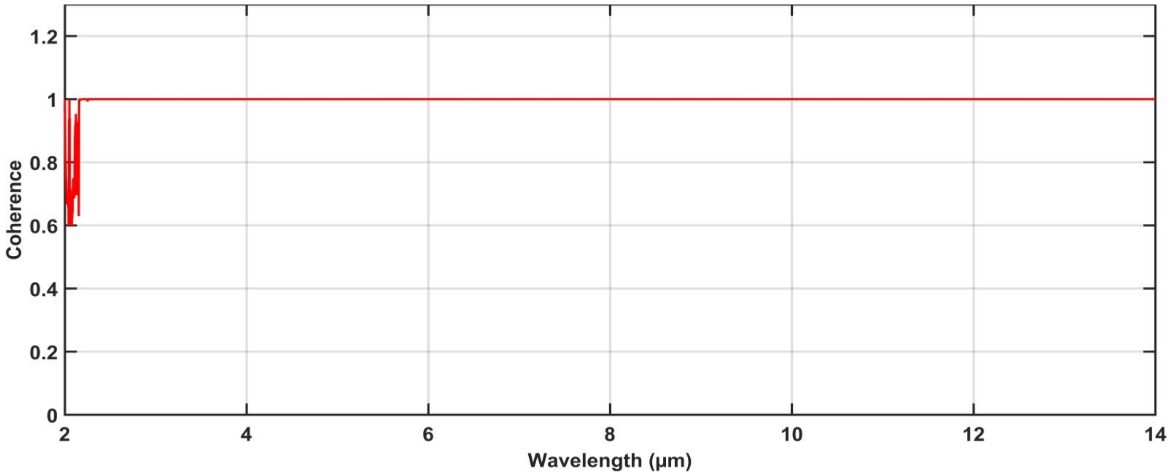

Fig. 10. Illustrates the SC spectral coherence in a 15 mm PCF, achieved using a 5.8 μm pump, 50 fs pulse duration (T_{FWHM}), and 15 kW peak power

Finally, we have investigated the impact of the material loss on the bandwidth of the generated SC spectra. Fig. 11 shows the output SC spectrum for an input laser pulse with a peak power and FWHM of 15 kW and 50 fs, respectively, where the optical attenuation due to the material loss is considered. The transmission spectrum is experimentally measured for a 15 mm thick of the GAST glass sample and the loss coefficient is estimated to be 0.17 dB/mm [58]. Compared to the previous case where the loss is not incorporated in simulations, the generated SC spectrum bandwidth at the spectral flatness level of less than 10 dB is reduced only by less than 1 μm. Moreover, this spectral narrowing can be easily compensated by increasing the peak power of the input optical pulses.

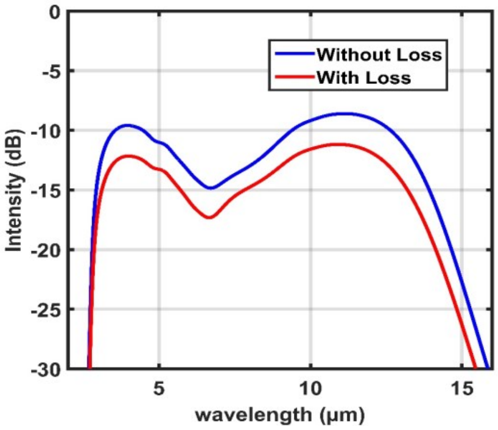

Fig. 11. SC generated with an input optical laser pulse peak power and FWHM of 15 kW and 50 fs, respectively with and without taking into account propagation material loss (colour online)

4. Conclusion

In summary, we have presented and discussed the numerical analysis of SC generation in PCF based on $Ge_{20}As_{20}Se_{17}Te_{43}$ chalcogenide in all-normal dispersion regime (ANDi). This CL-PCF is described by six rings of air holes. Based on the CL-PCF's high nonlinear refractive index and attractive dispersion properties. The results show that this material has tremendous potential for generating a broad supercontinuum with excellent coherence in the mid-infrared. We are using a pump with a wavelength of 5.8 µm and a pulse duration of 50 femtoseconds and 15 kW for the peak power, the results highlight the material and CL-PCF design potential for producing a broad and stable SC that extends from 2.9 to 13.95 µm only at -5 dB spectral level. This is especially important in the mid-infrared spectrum. Owing to the favorable properties of $Ge_{20}As_{20}Se_{17}Te_{43}$ chalcogenide glass, such as the high Kerr nonlinearity (γ = 1,495 $m^{-1}\cdot W^{-1}$) with a wavelength of 5.8 µm, in addition to its broad transparency range. Future studies can focus on further refining fiber designs to maximize efficiency and coherence, as well as validating the numerical predictions through experimental work. Overall, the insights from this investigation provide a valuable contribution to the development of new nonlinear optical devices based on chalcogenide photonic crystal fibers, paving the way for future advancements in mid-infrared SC sources.

Acknowledgements

The authors wish to acknowledge the Algerian Ministry of Higher Education and Scientific Research, as well as the Directorate-General for Scientific Research and Technological Development (DGRSDT), for their great support.

References

[1] R. Alfano, The Supercontinuum Laser Source: The Ultimate White Light, Springer, New York, 33–101 (2016).
[2] J. M. Dudley, G. Genty, S. Coen, Reviews of Modern Physics **78**(4), 1135 (2006).
[3] H. Xu, C. Zhao, W. Wu, S. Chen, Z. Jiang, Optoelectron. Adv. Mat. **13**, 182 (2019).
[4] A. Labruyère, A. Tonello, V. Couderc, G. Huss, P. Leproux, Optical Fiber Technology **18**, 375 (2012).
[5] K. E. Jahromi, Q. Pan, L. Høgstedt, S. M. Friis, A. Khodabakhsh, P. M. Moselund, F. J. Harren, Optics Express **27**(17), 24469 (2019).
[6] L. C. Van, H. Van Le, N. D. Nguyen, N. V. T. Minh, Q. H. Dinh, T. N. Thi, B. C. Van, Laser Physics **32**(5), 055102 (2022).
[7] L. E. Hooper, P. J. Mosley, A. C. Muir, W. J. Wadsworth, J. C. Knight, Optics Express **19**(6), 4902 (2011).
[8] A. Medjouri, D. Abed, Z. Becer, Opto-Electronics Review **27**(1), 1 (2019).
[9] C. Huang, M. Liao, W. Bi, X. Li, L. Hu, L. Zhang, W. Gao, Photonics Research **6**(6), 601 (2018).
[10] A. M. Heidt, J. Opt. Soc. Am. B **27**(3), 550 (2010).
[11] I. B. Gonzalo, R. D. Engelsholm, M. P. Sørensen, O. Bang, Scientific Reports **8**(1), 6579 (2018).
[12] A. M. Heidt, A. Hartung, G. W. Bosman, P. Krok, E. G. Rohwer, H. Schwoerer, H. Bartelt, Optics Express **19**(4), 3775 (2011).
[13] G. P. Agrawal, Nonlinear Fiber Optics, Springer, Berlin, pp. 195-211 (2000).
[14] J. H. Price, X. Feng, A. M. Heidt, G. Brambilla, P. Horak, F. Poletti, D. J. Richardson, Optical Fiber Technology **18**(5), 327 (2012).
[15] P. S. Maji, P. R. Chaudhuri, Optik **125**(20), 5986 (2014).
[16] H. Balani, G. Singh, M. Tiwari, V. Janyani, A. K. Ghunawat, Applied Optics **57**(13), 3524 (2018).
[17] D. Wang, X. Shen, Z. Wu, X. Wang, J. Yuan, X. He, C. Yu, Optoelectron. Adv. Mat. **11**, 616 (2017).
[18] J. Li, J. Wang, Y. Teng, Z. Xu, J. Cheng, Optical and Quantum Electronics **52**(10), 1 (2020).
[19] Y. Yuan, K. Xia, Y. Wang, Z. Liu, N. Zhang, J. Su, S. Dai, Optical Materials Express **9**(5), 2196 (2019).
[20] T. S. Saini, R. K. Sinha, Progress in Quantum Electronics **78**, 100342 (2021).
[21] R. E. Slusher, G. Lenz, J. Hodelin, J. Sanghera, L. B. Shaw, I. D. Aggarwal, J. Opt. Soc. Am. B **21**(6), 1146 (2004).
[22] T. M. Monro, Y. D. West, D. Hewak, N. G. R. Broderick, D. J. Richardson, Journal of Lightwave Technology **18**(12), 50 (2000).
[23] M. Zhang, L. Li, T. Li, F. Wang, K. Tian, H. Tao, Z. Yang, Optics Express **27**(20), 29287 (2019).
[24] M. Diouf, L. M. Mandeng, C. Tchawoua, M. Zghal, Journal of Lightwave Technology **37**(22), 5692 (2019).
[25] T. S. Saini, A. Kumar, R. Kumar Sinha, Optics Communications **347**, 13 (2015).
[26] P. Yan, R. Dong, G. Zhang, H. Li, S. Ruan, H. Wei, J. Luo, Optics Communications **293**, 133 (2013).
[27] S. A. Seyed Hashemi, M. Noori, Physica Scripta **95**(7), 075501 (2020).
[28] M. Diouf, A. ben Salem, R. Cherif, H. Saghaei, A. Wague, Applied Optics **56**(2), 163 (2017).
[29] M. Diouf, R. Cherif, A. ben Salem, A. Wague, Journal of Modern Optics **64**(13), 1335 (2017).
[30] M. R. Karim, B. M. A. Rahman, Applied Physics Research **8**(4), 29 (2016).
[31] A. Medjouri, D. Abed, Optik **219**, 165178 (2020).
[32] H. Ou, S. Dai, P. Zhang, Z. Liu, X. Wang, F. Chen, R. Wang, Optics Letters **41**(14), 3201 (2016).
[33] B. J. Eggleton, B. Luther-Davies, K. Richardson, Nature Photonics **5**(3), 141 (2011).
[34] A. Lemiere, F. Désévédavy, P. Mathey, P. Froidevaux, G. Gadret, J. C. Jules, F. Smektala, J. Opt. Soc. Am. B **36**(2), 183 (2019).
[35] S. Cherukulappurath, M. Guignard, C. Marchand, F. Smektala, G. Boudebs, Opt. Commun. **242**(1–3), 313 (2004).

[36] Z. Yang, T. Luo, S. Jiang, J. Geng, P. Lucas, Opt. Lett. **35**(20), 3360 (2010).

[37] Z. Zhao, X. Wang, S. Dai, Z. Pan, S. Liu, L. Sun, R. Wang, Opt. Lett. **41**(22), 5222 (2016).

[38] J. Xiao, Y. Tian, Z. Zhao, J. Yao, X. Wang, P. Chen, R. Wang, Opt. Fiber Technol. **55**, 102144 (2020).

[39] K. Jiao, J. Yao, Z. Zhao, X. Wang, N. Si, X. Wang, R. Wang, Opt. Express **27**(3), 2036 (2019).

[40] A. Medjouri, L. M. Simohamed, O. Ziane, A. Boudrioua, Z. Becer, Photonics Nanostructures-Fundamentals and Applications **16**, 43 (2015).

[41] S. Guo, F. Wu, S. Albin, H. Tai, R. S. Rogowski, Opt. Express **12**(15), 3341 (2004).

[42] W. Su, S. Lou, H. Zou, B. Han, Infrared Phys. Technol. **63**, 62 (2014).

[43] A. Medjouri, D. Abed, Optical Engineering **61**(9), 096106 (2022).

[44] L. C. Van, T. N. Thi, B. T. L. Tran, D. H. Trong, N. V. T. Minh, H. V. Le, V. T. Hoang J. Photonics Nanostruct. Fundam. Appl. **48**, 100986 (2022).

[45] C. C. Wang, W. M. Li, N. Li, W. Q. Wang, Opt. Laser Technol. **88**, 215 (2017).

[46] H. Ahmad, M. R. Karim, B. M. A. Rahman, Appl. Phys. B **124**, 1 (2018).

[47] B. Siwicki, M. Klimczak, R. Stępień, R. Buczyński, Opt. Fiber Technol. **25**, 64 (2015).

[48] J. Hult, J. Light Wave Technol. **25**(12), 3770 (2007).

[49] G. P. Agrawal, Nonlinear fiber optics, Springer, Berlin, 195-211 (2000).

[50] P. S. Maji, P. R. Chaudhuri, Appl. Opt. **54**(13), 4042 (2015).

[51] P. Munsaka, P. Baricholo, E. G. Rohwer, G. W. Bosman, Opt. Continuum. **2**(1), 9 (2023).

[52] A. Medjouri, D. Abed, Opt. Quantum Electron. **53**, 1 (2021).

[53] J. R. Martinez-Angulo, J. C. Hernandez-Garcia, J. H. Barron-Zambrano, J. M. Estudillo-Ayala, O. Pottiez, J. P. Lauterio-Cruz, R. Rojas-Laguna, Results Phys. **15**, 102613 (2019).

[54] M. Brehler, M. Schirwon, D. Göddeke, P. M. Krummrich, J. Lightwave Technol. **35**(17), 3622 (2017).

[55] J. M. Dudley, S. Coen, Opt. Lett. **27**(13), 1180 (2002).

[56] H. P. T. Nguyen, T. H. Tuan, L. Xing, M. Matsumoto, G. Sakai, T. Suzuki, Y. Ohishi, Opt. Express **28**(12), 17539 (2020).

[57] Z. Zhang, D. T. Reid, S. C. Kumar, M. Ebrahim-Zadeh, P. G. Schunemann, K. T. Zawilski, C. R. Howle, Opt. Lett. **38**, 5110 (2013).

[58] F. Xiao, W. Sun, X. Liang, J. Jia, M. Zhang, X. Wan, K. Jiao, S. Bai, L. Wang, S. Dai, Q. Nie, X. Shen, R. Wang, X. Wang, Opt. Mater. Express **13**(12), 3445 (2020).

---

[*] Corresponding author: medjouri-abdelkader@univ-eloued.dz